npj | Quantum Materials

www.nature.com/npjquantmats

ARTICLE OPEN

Domain imaging across the magneto-structural phase transitions in $Fe_{1+y}Te$

Jonas Warmuth[1], Martin Bremholm[2], Philip Hofmann[3], Jens Wiebe[1] and Roland Wiesendanger[1]

The investigation of the magnetic phase transitions in the parent compounds of Fe-based superconductors is regarded essential for an understanding of the pairing mechanism in the related superconducting compounds. Even though the chemical and electronic properties of these materials are often strongly inhomogeneous on a nanometer length scale, studies of the magnetic phase transitions using spatially resolved experimental techniques are still scarce. Here, we present a real space spin-resolved scanning tunneling microscopy investigation of the surface of $Fe_{1+y}Te$ single crystals with different excess Fe content, y, which are continuously driven through the magnetic phase transition. For $Fe_{1.08}Te$, the transition into the low-temperature monoclinic phase is accompanied by the appearance of a chevron-patterned structural ordering due to the four 90° rotational domains of the monoclinic lattice. Each of the structural domains contains locally commensurate nanoscale diagonal double stripe antiferromagnetic spin order domains with π-phase slips accross domain boundaries. In the low-temperature phase of $Fe_{1.12}Te$, on the other hand, the chevron pattern gets rather narrow and less well-defined, and an additional 90° rotated component of the spin-order with local plaquette order emerges. The simultaneous imaging of spin and structural order we show here gives valuable insights into the nature of the magneto-structural domains of $Fe_{1+y}Te$ near the tricritical point, which presumably add to the understanding of the mechanism of superconductivity in the related $Fe_{1+y}Te_xSe_{1-x}$ material.

npj Quantum Materials (2018)3:21 ; doi:10.1038/s41535-018-0096-1

INTRODUCTION

$Fe_{1+y}Te$ is the non-superconducting parent compound of $Fe_{1+y}Se_xTe_{1-x}$, in which superconductivity is induced by the substitution of Te with Se.[1] These Fe-chalcogenides form the structurally simplest material group of all Fe-based superconductors and they are therefore the ideal compound for a fundamental investigation of the complex mechanisms leading to superconductivity in these materials.[2–9] So far, the complex interplay of competing spin orders[10–15] and structural phase transitions in $Fe_{1+y}Te$, which crucially depends on the amount y of excess Fe, has been mostly investigated by spatially averaging techniques, such as neutron diffraction, magnetic susceptibility, and resistivity measurements.[7,8,16] For low values of excess Fe, $y < 0.11$, a simultaneous magnetic and structural, so called magneto-structural, transition from a high-temperature paramagnetic tetragonal ($\mathcal{T}$) to a low-temperature monoclinic ($\mathcal{M}$) phase with a diagonal double stripe (DDS) antiferromagnetic spin order[17] was observed. The transition temperature of this phase transition decreases with increasing y. For $y > 0.13$ there is an intermediate magneto-structural transition from the $\mathcal{T}$ phase into an incommensurate helimagnetic orthorhombic ($\mathcal{O}$) phase upon cooling,[18,19] with indications of local instability toward plaquette order.[20] Most notably, for an excess Fe content of $0.11 \leq y \leq 0.13$ there are indications of a tricritical point,[8] and the microscopic nature of the complex interplay between structural, magnetic, and electronic phases in this critical regime have been discussed controversially. References [8,21] interpreted their observations with a coexistence of two different structural and magnetic phases, i.e., a $\mathcal{M}$ and an $\mathcal{O}$ phase with almost commensurate spin-density wave-like order and incommensurate helical spin-order, where the phase separation has been ascribed to be of electronic origin. This peculiar mixed phase was moreover predicted within an orbital ordering double exchange model.[22] In stark contrast, refs. [16,23] interpret their data with a single structural phase with lower symmetry than $\mathcal{M}$ explained by a bond-order wave transition, separate from the magnetic and structural transitions, which is related to ferro-orbital ordering.

Former studies using spatially resolved techniques focused on the investigation of the magnetic components of the $\mathcal{T}$ to $\mathcal{M}$ transition in the regime $y < 0.11$, as well as on the $\mathcal{O}$ phase in the regime $y > 0.13$ with spin-resolved scanning tunneling microscopy (SP-STM).[20] For the $\mathcal{M}$ phase, a twinning of the DDS spin structure into two domains rotated by 90° was revealed. For $y = 0.15$, the SP-STM images indicated coexistence of two DDS orders mutually rotated by 90° and local instability toward plaquette order. To the best of our knowledge, neither the structural components of the $\mathcal{T}$ to $\mathcal{M}$ magneto-structural phase transition in the regime $y < 0.11$, nor the complex consecutive phase transitions in the regime $0.11 \leq y \leq 0.13$ have been studied on a local scale. Here, we report continuous temperature-dependent STM measurements mapping the magneto-structural phase transition of $Fe_{1+y}Te$ in real space. We investigated $Fe_{1+y}Te$ samples with two different excess Fe contents, $y = 0.08$ and $y = 0.12$, determined from single crystal X-ray diffraction (SC-XRD, see Methods section), such that the former is expected to have a low-temperature $\mathcal{M}$ phase, while the latter has a composition close to the intriguing tricritical point.[8] The experimental methods used for the sample preparation,

[1]Department of Physics, Hamburg University, 20355 Hamburg, Germany; [2]Department of Chemistry, Interdisciplinary Nanoscience Center (iNANO), Aarhus University, 8000 Aarhus, Denmark and [3]Department of Physics and Astronomy, Interdisciplinary Nanoscience Center (iNANO), Aarhus University, 8000 Aarhus, Denmark
Correspondence: Jonas Warmuth (jwarmuth@physnet.uni-hamburg.de) or Jens Wiebe (jwiebe@physnet.uni-hamburg.de)

Received: 30 November 2017 Revised: 15 March 2018 Accepted: 26 March 2018
Published online: 18 April 2018

characterization, and the used experimental techniques of magnetic susceptibility measurements and SP-STM are described in the Methods section.

RESULTS

The temperature dependence of the magnetic susceptibility of the sample with the lower content of excess Fe ($Fe_{1.08}Te$) reveals a sharp transition at $T_N \approx 65$ K with only a small thermal hysteresis ($\Delta T \approx 1$ K) between the cooling and heating cycles (Fig. 1a). As shown in ref.[8] and corroborated by the shape of the magnetic susceptibility, the relatively low Fe content is expected to result in a simultaneous first-order magnetic and structural transition from the $\mathcal{T}$ into the $\mathcal{M}$ phase upon cooling. In order to image this transition in real space, the surface of the $Fe_{1.08}Te$ single crystal is investigated with temperature-dependent SP-STM. In the high-temperature $\mathcal{T}$ phase (Fig. 1c), the surface is atomically flat apart from step edges with a height of an FeTe layer with a thickness of one unit cell (see upper left corner of Fig. 1c and line profile in Fig. 1d). In strong contrast, in the low-temperature $\mathcal{M}$ phase, the surface decomposes into diamond-shaped domains of hundreds of nanometer dimensions, which form a chevron pattern (Fig. 1b, e). Within the domains, the surface is still atomically flat, but the surface normal vectors have four different orientations corresponding to four different domain types classified by colors in Fig. 1b. The surface normal of the green, yellow, blue, and red domain types are tilted by 0.81° ± 0.04° with respect to the overall surface normal toward the four cardinal crystallographic directions of the $Fe_{1.08}Te$ single crystal. This leads to an increased apparent roughness of the surface as seen in the line profile in Fig. 1d.

In order to study the magnetic order within these domains, the surface is investigated by atomically resolved SP-STM across the domain boundaries (Fig. 2a, b). As shown in Fig. 2b, as well as in the zoomed images in Fig. 2c, d, the well-known stripe-shaped DDS spin-contrast[17] with a periodicity of $2a$ is visible in all four different domains of the $\mathcal{M}$ phase. However, there are two different orientations of the stripes, as seen most clearly from the fast Fourier transforms (FFTs) selectively taken from surface areas in the four domains (insets in Fig. 2c, d; c is rotated by 45° with respect to d). Note that the angle between q_a and q_b differs from 90° due to residual lateral temperature drift and scanner creep effects in the STM images (see Methods section). Moreover, the q_{AFM} peaks appear rather blurry because of the small image area, and because of a nanoscale domain formation which will be investigated in detail below. While the stripes in the red and yellow domain types are roughly oriented at a polar angle of 45°, they are oriented at 135° in the blue and green domain types. Since the stripe-shaped contrast can be assigned to the DDS spin order of $Fe_{1+y}Te$,[17] we can conclude that the DDSs have the same orientation in the red and yellow domains, but are rotated by about 90° with respect to this orientation in the green and blue domains. This leads to two different types of domain boundaries; one where the orientation of the DDSs is not changing (A-type domain boundary between red and yellow, or blue and green domains, e.g., Fig. 2c), and one where the DDSs are rotating by about 90° (B-type domain boundary between yellow and green, or red and blue domains, e.g., Fig. 2d). Obviously, the surface domain-types and the magnetic orientations are interconnected and we presume that the formation of the four domain types is due to the magneto-structural phase transition in the $Fe_{1.08}Te$ sample.

This conclusion is further substantiated by a structural model (Fig. 3). Since the DDSs are known to be oriented along the lattice vector b, we can determine the a- and b-directions within the four different domains, as shown by the arrows in Fig. 2c, d. Note that these directions principally are still indeterminated concerning rotation by 180° using the SP-STM contrast, but we can assign the absolute orientations from the following model. In the $\mathcal{T}$ phase

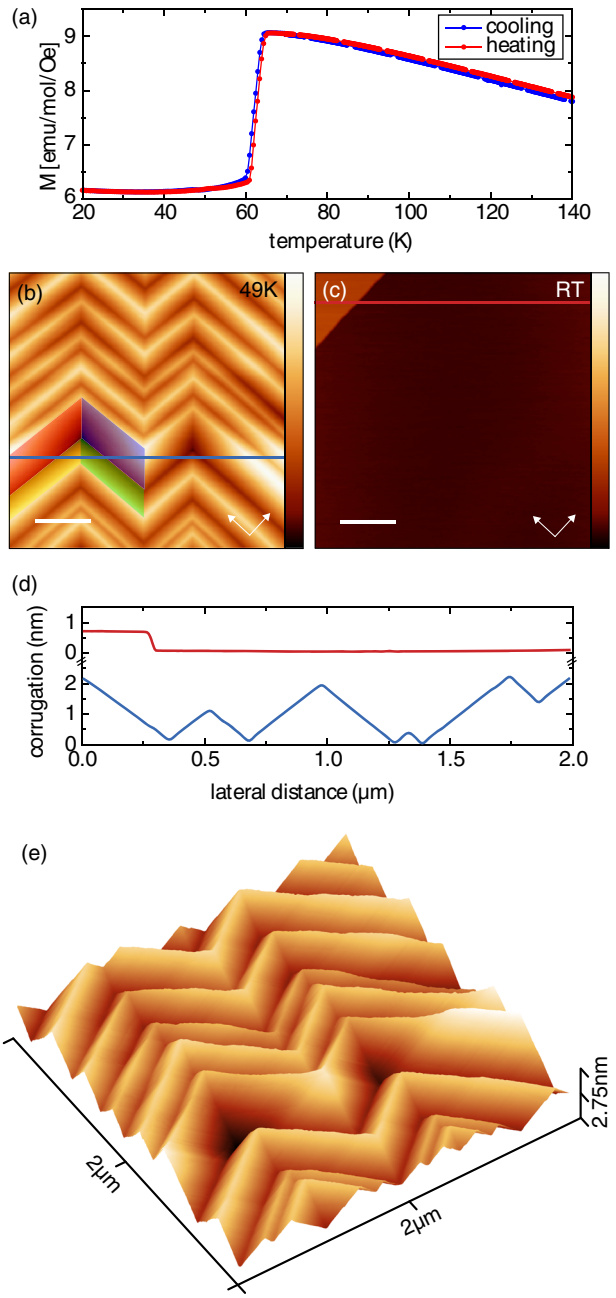

Fig. 1 Surface morphologies of the $\mathcal{M}$ and $\mathcal{T}$ phases of $Fe_{1.08}Te$. **a** Magnetic susceptibility of $Fe_{1.08}Te$ measured in a field of 0.1 T as a function of temperature for the cooling (blue) and heating (red) cycle. The magneto-structural phase transition appears at $T_N \approx 65$ K. **b** Constant-current STM image of the surface of $Fe_{1.08}Te$ taken at $T = 49$ K in the $\mathcal{M}$ phase ($V_s = 100$ mV, $I_t = 40$ pA, scale bar width 400 nm, color scale from 0 (black) to 2.75 nm (white)). Four domains of different types are marked by color. **c** Constant-current STM image of the surface of $Fe_{1.08}Te$ taken at room temperature in the $\mathcal{T}$ phase ($V_s = 500$ mV, $I_t = 20$ pA, scale bar width 400 nm, color scale from 0 (black) to 2.75 nm (white)). **d** Line profiles taken along the lines marked in **b**, **c**. **e** Three-dimensional view of the surface of $Fe_{1.08}Te$ shown in **b**

the four rotational domains, which can be generated by 90° rotations of the $\mathcal{T}$ lattice around the c-axis are degenerate (Fig. 3a). However, this is not the case for the $\mathcal{M}$ phase (Fig. 3b). Here, the four 90° rotations of the $\mathcal{M}$ lattice result in four distinguishable orientations, which are shown in Fig. 3c. Each of the four

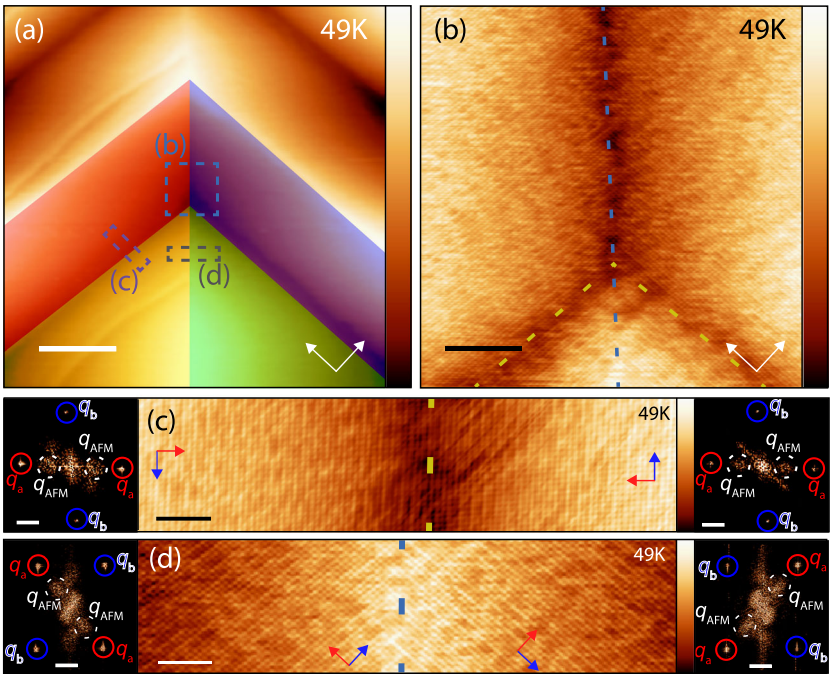

Fig. 2 Magnetic imaging of the structural domains of the $\mathcal{M}$ phase of $Fe_{1.08}Te$. All SP-STM images were recorded at $T = 49$ K. **a** Overview constant-current STM image of an area of the $\mathcal{M}$ phase of $Fe_{1.08}Te$ with four domains of different types marked by different colors. The dashed boxes indicate the areas where the images **b**–**d** were taken ($V_s = 300$ mV, $I_t = 40$ pA, scale bar width 60 nm, color scale from 0 (black) to 1 nm (white)). **b** SP-STM image of the area marked in **a** showing the intersection of four structural domains resulting in two A-type (dashed yellow lines) and two B-type (dashed blue lines) structural domain boundaries ($V_s = -100$ mV, $I_t = 100$ pA, scale bar width 8 nm, color scale from 0 (black) to 3 Å (white)). The arrows in **a**, **b** indicate the lattice directions of the unit cell. **c** SP-STM image of the area marked in **a** with an A-type boundary (yellow dashed line) between a red (left side) and a yellow (righ side) domain type ($V_s = -100$ mV, $I_t = 106$ pA, scale bar width 4 nm, color scale from 0 (black) to 3 Å (white)). Note that the image is rotated by 45° with respect to **a**, **b**, **d**. **d** SP-STM image of the area marked in **a** with a B-type boundary (blue dashed line) between a yellow (left side) and a green (right side) domain type ($V_s = -100$ mV, $I_t = 102$ pA, scale bar width 4 nm, color scale from 0 (black) to 2.5 Å (white)). The red and blue arrows in **c**, **d** indicate the directions of the *a* and *b* lattice vectors, respectively. The insets in **c**, **d** represent the FFTs of the left and right sides of the images, scale bars are 6 nm^{-1}. Red, blue, and dashed white circles surround the Bragg peaks q_a and q_b and the peaks q_{AFM} due to the DDS spin structure, respectively

orientations has a distinct normal vector of the (*a*, *b*)-plane. We therefore tentatively conclude that the four domains observed at the surface in the STM images are due to four rotational structural domains of the crystal, where in each domain the lattice is given by one of the four orientations shown in Fig. 3c. This is finally corroborated by a comparison of the expected and measured angles between the local surfaces in each of the four domains. Line profiles taken perpendicularly across B-type (Fig. 3f, g) and A-type (Fig. 3f, h) boundaries, respectively, reveal angles of $\delta_{STM} = 178.93° \pm 0.04°$ and $2\beta_{STM} = 178.38° \pm 0.08°$ (averages of 15 line profiles, the error in δ_{STM} is dominated by the 5% uncertainty in the calibration of the STM). The according angles expected within the structural model of Fig. 3c are $2\beta = 178.55° \pm 0.13°$ known from neutron and X-ray powder-diffraction of $Fe_{1+y}Te$ with similar excess Fe content,[24,25] and $\delta = -(\cos^{-1}(\cos^2\beta \cdot \cos\theta + \sin^2\beta) - 180°)$, which depends on the rotation θ between the red and blue domain. β_{STM} is in excellent agreement with the diffraction data. For the determination of δ, we need to consider that θ is not exactly 90° because of the difference in the *a* and *b* lattice constants (Fig. 3e), which will also induce strain in the B-type boundary. While it is a complex problem to predict the resulting θ from the model, we can still measure θ_{STM} from the experimental data as the angle between A-type boundaries (Fig. 3f), which results in $\theta_{STM} = 104° \pm 10°$ (average from 15 measurements, the error is dominated by a 10% uncertainty due to lateral drift and creep effects of the STM tip). Note that these measurements have been done using similar images as that shown in Fig. 3f, but taken at 32 K where the STM is most stable and the length calibration is most accurate. Indeed θ is considerably larger than 90°. The resulting calculated $\delta = 178.85° \pm 0.15°$ (based on β and θ_{STM}) is consistent with the measured value given above. We can therefore conclude that the observed domains are indeed the four rotational structural domains illustrated in Fig. 3c.

The identity between structural and magnetic domains shown above enables measurements of the magneto-structural domains during cooling or heating across the magneto-structural phase transition without the need of spin-resolution in STM, as will be shown in the following. Figure 4a illustrates an STM image of the surface of the $Fe_{1.08}Te$ sample, which has been taken while cooling the sample from a temperature slightly above to a temperature slightly below the critical temperature using a constant cooling rate. Since the cooling rate (0.1 K min^{-1}) is very slow as compared to the scan rate (2.66 s per line) the temperature decreases by less than 5 mK in each scan line from bottom to top. In the $\mathcal{T}$ phase (bottom of Fig. 4a and black line profile in Fig. 4c) the surface is atomically flat. When approaching the phase transition, the surface starts to show some waviness in the diagonal direction with a characteristic length scale of ≈1 µm (center of Fig. 4a and red line profile in Fig. 4c). Finally, at $T = 64.4$ K, the imaged sample area passes over into the $\mathcal{M}$ phase as indicated by the sudden appearance of the strong corrugation in the blue line profile in Fig. 4c, which is due to the magneto-structural domains (top of Fig. 4a). This transition happens within a single scan line, i.e., in a temperature interval on the order of only 5 mK. However, due to the slow scanning, we cannot determine the time it takes for the whole image area to transition into the $\mathcal{M}$ phase. A similar experiment is shown in Fig. 4b, but now during heating of the sample across the phase transition while scanning from top to bottom. Note that the area is exactly the same as in Fig. 4a as indicated by the defects used as markers (see ellipses).

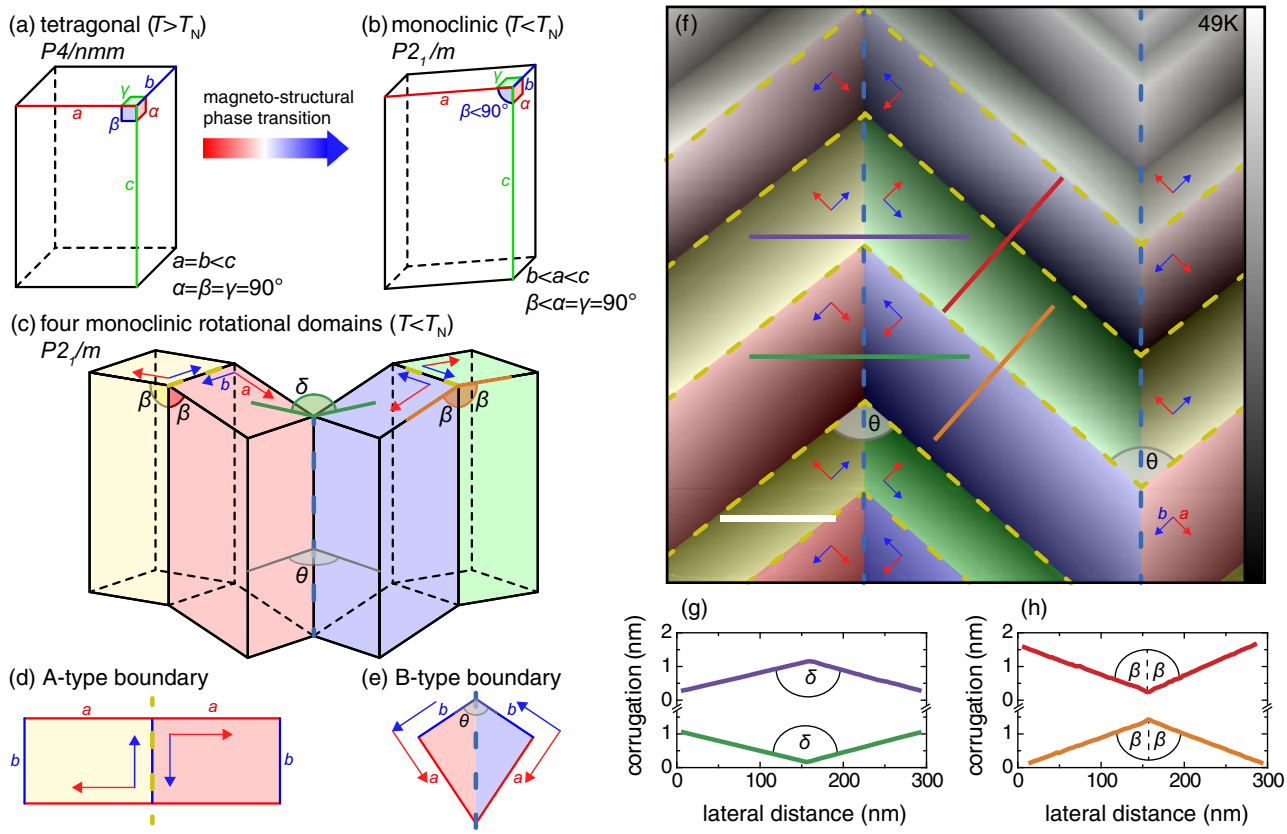

Fig. 3 Structural models of $Fe_{1+y}Te$ in the $\mathcal{T}$ and $\mathcal{M}$ phases. **a**, **b** Simplified unit cell models for the $\mathcal{T}$ phase (**a**) and for the $\mathcal{M}$ phase (**b**) with the indicated directions of the *a*, *b*, and *c* lattice vectors and the corresponding angles. **c** Illustration of the proposed structural model for the $\mathcal{M}$ phase of $Fe_{1.08}Te$ with four rotational domains composed of unit cells which are rotated by 0° (yellow), 180° (red), θ (blue), and $\theta + 180°$ (green). Vectors in the direction of *a* (red), and *b* (blue), as well as the definition of the angles β and δ are indicated. **d**, **e** Top views of the A-type (**d**) and B-type (**e**) structural domain boundaries (same domain colors, vectors and angles as in **c**). **f** Constant-current STM image of the surface of $Fe_{1.08}Te$ below T_N overlayed with a color map marking the four rotational structural domains with the same colors as in **c** ($V_s = 300$ mV, $I_t = 40$ pA, scale bar width 200 nm, color scale from 0 (black) to 3.2 nm (white)). The dashed yellow and blue lines mark the A- and B-type boundaries, respectively. The angle θ between A-type boundaries is indicated. **g**, **h** Profiles perpendicular across two B-type (**g**) and two A-type (**h**) boundaries. The profiles were taken along the lines which are marked with the identical colors in **f**. The extracted angles δ and β are indicated

The corresponding line profiles directly before and after the phase transition are given in Fig. 4d as blue and red lines, respectively. Again, the transition happens very abruptly in one scan line. However, now, the transition temperature is considerably higher ($T = 67.0$ K) as for the cooling cycle. Obviously, this thermal hysteresis ($\Delta T \approx 2.5$ K) for the phase transition of the small imaged surface area is of a similar size as that of the macroscopic sample determined from the susceptibility measurements given above (Fig. 1a). Interestingly, the long-scale waviness of the surface in the $\mathcal{T}$ phase, which was found as a precursor of the phase transition for the cooling cycle, is not visible after the transition from the $\mathcal{M}$ into the $\mathcal{T}$ phase in the heating cycle (bottom of Fig. 4b and red line profile in Fig. 4d). This precursor is probably a strongly strained $\mathcal{T}$ phase, which is not present in the heating cycle because of the increased temperature due to thermal hysteresis.

Interesting questions are, whether the arrangement of the magneto-structural domains is affected by the surface, and whether it changes after consecutive phase transitions. In order to investigate these questions, we took an STM image of a sample area which is crossed by a step edge of a unit cell height in the $\mathcal{M}$ phase, heated into the $\mathcal{T}$ phase, cooled back into the $\mathcal{M}$ phase, and imaged the same area (Fig. 4e, f). Obviously, the arrangement of the magneto-structural domains changed drastically after cycling the sample once through the phase transition. While the chevron pattern of the domain structure is running vertically in Fig. 4e, it runs horizontally in Fig. 4f, indicating a 90° rotation of the B-type domain boundaries. Moreover, the length of the domains has changed, as visible from the increased separation of the B-type domain boundaries in Fig. 4f as compared to Fig. 4e. Also, the domain width is considerably decreased in the images of Fig. 4e, f, which were taken after cycling the sample slowly through the phase transition, as compared with the more virgin sample in Figs. 1b and 4f. Although this has not been investigated systematically, it indicates that slow cooling of the sample through the phase transition decreases the domain width. Finally, there is no obvious effect of the step edge on the domain arrangement, indicating that the surface and their defects have a negligible impact on the magneto-structural domain configuration, which is a bulk phenomenon.

In the following, we investigate the effect of the critical excess Fe content $y = 1.12$ on the structural and spin order by imaging the domains at the surface of a $Fe_{1.12}Te$ sample across the magnetic phase transition (Fig. 5). The temperature dependence of the magnetic susceptibility of this sample (Fig. 5a) reveals a much broader phase transition starting at a lower $T_N \approx 59$ K, as compared with the $Fe_{1.08}Te$ sample (cf. Fig. 1a). Moreover, there is an additional shoulder at lower temperature showing a strong thermal hysteresis in the cooling and heating cycles of about $\Delta T \approx 10$ K. The characteristic shape of the susceptibility of the $Fe_{1.12}Te$ sample was previously interpreted by a two-step structural phase transition:[8] a second order transition from the $\mathcal{T}$ phase into an intermediate $\mathcal{O}$ phase ($T \approx 59$ K), followed by a first-order

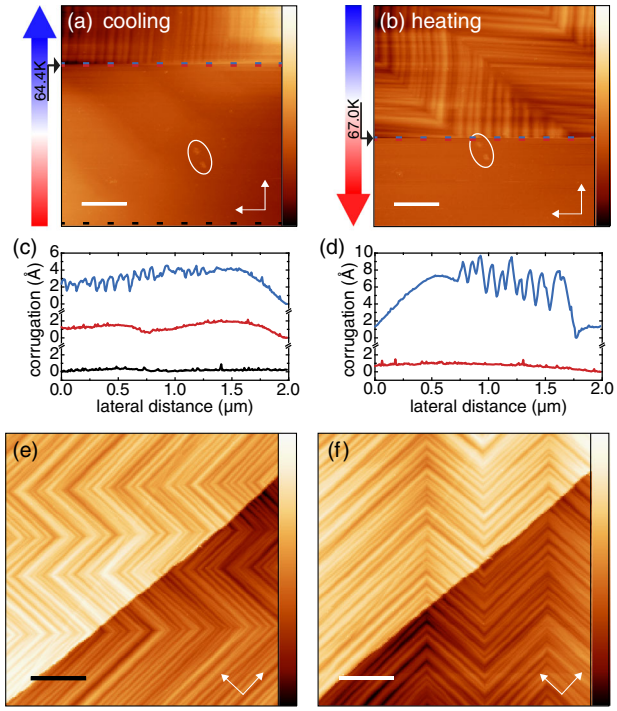

Fig. 4 Domain imaging across the magneto-structural phase transition of $Fe_{1.08}Te$. **a** Constant-current STM image of $Fe_{1.08}Te$ taken while decreasing the temperature with a rate of 0.1 K min^{-1} across the magneto-structural phase transition ($V_s = 300$ mV, $I_t =$ 40 pA, scale bar width 400 nm, color scale from 0 (black) to 3 nm (white), temperature scale from 65.4 K (red) to 64.3 K (blue)). The image is scanned from bottom to top, line by line in the horizontal direction, resulting in a linearly decreasing temperature as given by the temperature scale on the left. Each of the 256 lines takes a time of ≈2.66 s. The phase transition from the $\mathcal{T}$ (bottom) to the $\mathcal{M}$ (top) phase occurs at $T = 64.4$ K. **b** Same as **a**, but during increasing the temperature across the magneto-structural phase transition from the top to the bottom of the image (temperature scale from 66.6 K (blue) to 67.2 K (red)). The scanned area is the same as in **a** as indicated by the defects used as a marker (see ellipses in **a**, **b**). The phase transition from $\mathcal{M}$ (top) to $\mathcal{T}$ (bottom) phase occurs at $T =$ 67.0 K. **c**, **d** Height profiles in the $\mathcal{M}$ (blue) and $\mathcal{T}$ (red, black) phases for the cooling (**c**) and the heating (**d**) cycles, taken along the dashed lines marked with the corresponding color in **a**, **b**, respectively. Note that these profiles were taken from backward scans, i.e., from right to left. **e**, **f** Constant-current STM images of the identical surface area in the $\mathcal{M}$ phase of $Fe_{1.08}Te$, containing a step edge ($V_s = 300$ mV, $I_t = 40$ pA, scale bar width 300 nm, color scale from 0 (black) to 1.25 nm (white)). In between the images, the sample was heated into the $\mathcal{T}$ phase and cooled back into the $\mathcal{M}$ phase

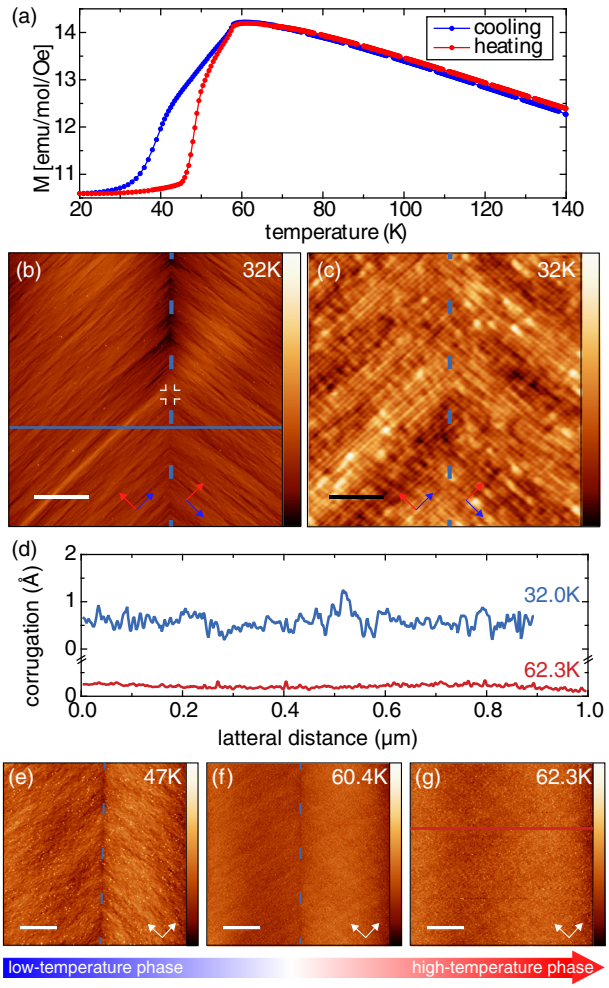

Fig. 5 Domain imaging across the magnetic phase transition of $Fe_{1.12}Te$. **a** Magnetic susceptibility of $Fe_{1.12}Te$ measured in a field of 0.1 T as a function of temperature for the cooling (blue) and heating (red) cycle. There is a rather broad phase transition starting at $T_N \approx$ 59 K. **b** Overview constant-current STM image of the sample surface in the low-temperature phase taken at $T = 32$ K ($V_s = 300$ mV, $I_t =$ 40 pA, scale bar width 180 nm, color scale from 0 (black) to 450 pm (white)). A B-type boundary is marked by the dashed vertical line. **c** SP-STM image taken at the same temperature close to the B-type boundary showing the DDS spin orders in the two domains, which are rotated by 90° with respect to each other ($V_s = -20$ mV, $I_t = 1$ nA, scale bar width 4 nm, color scale from 0 (black) to 100 pm (white)). **d** Blue and red height profiles perpendicular to the B-type boundary taken along the horizontal lines marked in **b**, **g**, respectively. **e**–**g** Constant-current STM images of an identical surface area taken across the phase transition at the indicated temperatures $T = 47$ K (**e**), $T = 60.4$ K (**f**), and $T = 62.3$ K (**g**). A B-type domain boundary is marked by the dashed vertical lines in **e**, **f**, but is now longer visible in **g** ($V_s = 300$ mV, $I_t = 40$ pA, scale bar width 200 nm, color scale from 0 (black) to 50 pm (white))

transition into the $\mathcal{M}$ structure, as indicated by the shoulder ($T \approx$ 40 K). The strong thermal hysteresis of this shoulder indicates a considerable sluggishness of the latter phase transition, which can be ascribed to a strong competition between $\mathcal{O}$ and $\mathcal{M}$ phases. Therefore, it was proposed that the low-temperature phase consists of a mixture of $\mathcal{O}$ and $\mathcal{M}$ phases with metastable states that can persist over long time periods.[8] Large-scale STM images in the low-temperature phase (Fig. 5b) reveal a much less ordered structure as compared to the chevron pattern of the $Fe_{1.08}Te$ sample (cf. Fig. 4f). In atomically resolved SP-STM images, we can still faintly observe a stripe-shaped spin-contrast (Fig. 5c) with a clear B-type boundary marked by the dashed vertical line that separates domains where the stripes run from top left to bottom right (left of the boundary) and from bottom left to top right (right of the boundary, see an in-depth investigation of the spin-order in Fig. 6). This B-type boundary is also well-defined on a large-length scale (dashed vertical line in Fig. 5b). However, there is no clear formation of a well-ordered chevron pattern with sharp and straight A-type boundaries, as in the case of the $Fe_{1.08}Te$ sample. Merely, an increased surface roughness is visible in the direction perpendicular to the spin-contrast stripes (Fig. 5d) with a periodicity of ≈8 nm, which leads to the stripy appearance of the STM image in Fig. 5b. When the sample is heated into the phase transition regime (Fig. 5e, f) the stripy contrast and the B-type boundary very gradually decrease in visibility, until the sample surface is finally atomically flat in the $\mathcal{T}$ phase (Fig. 5d, g).

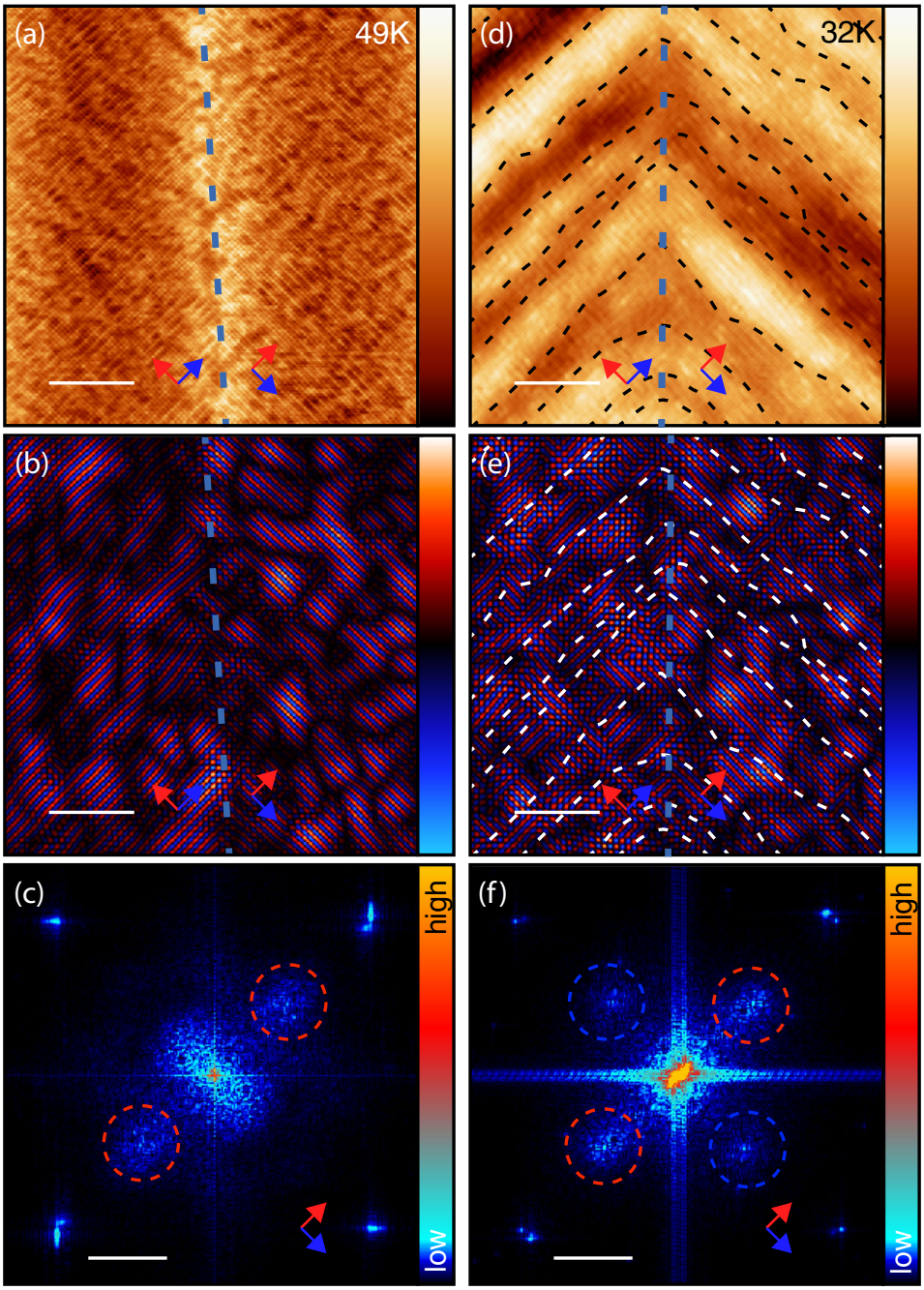

Fig. 6 Comparison of the spin structures of $Fe_{1.08}Te$ (left) and $Fe_{1.12}Te$ (right). **a**–**c** $Fe_{1.08}Te$: SP-STM image (**a**) across a B-type domain boundary (dashed blue line), its FFT (**c**, overlay of the FFT of the right domain and of the left rotated by 90°), and inverse FFT (**b**) of **c** after application of a gaussian filter passing only the spin contrast (red dashed circles in **c**). Measurement parameters are $V_s = -100$ mV, $I_t = 10$ pA, $T = 49$ K, scale bar width for **a**, **b** 8 nm, color scale for **a** from 0 (black) to 295 pm (white), for **b** from 0 (blue side) to 40 pm (red side). **d**–**f** same as **a**–**c**, but for $Fe_{1.12}Te$. The dashed black lines in **d**, **e** trace the contour lines of the constant-current SP-STM image in **d**. The dashed blue circles in **f** mark the additional spots due to a component of the spin order which, in both domains, is rotated by 90° with respect to the usual direction (dashed red circles). Measurement parameters are $V_s = -100$ mV, $I_t = 30$ pA, $T = 32$ K, color scale for **d** from 0 (black) to 270 pm (white), for **e** from 0 (blue side) to 18 pm (red side). Scale bar for the FFT images **c**, **f** is 6 nm^{-1}

This gradual process might be related to the proposed transition into the $\mathcal{O}$ phase.[8]

In order to investigate the spin-order in this excess Fe regime in detail and compare with the lower-doped sample, we show in Fig. 6 an analysis of atomically resolved SP-STM images using Fourier filtering. Large scale atomically resolved SP-STM images taken in the low-temperature phases of both materials across a B-type domain boundary again illustrate the strongly reduced width and irregularity of the structural chevron pattern in the critical doping regime (see dashed lines in Fig. 6d, the chevron in the low -doped sample is much larger than the image area of Fig. 6a). Figure 6c shows an FFT of Fig. 6a from the area to the right of the B-type domain boundary summed up with an FFT from the area to the left, but rotated by 90° before summation, revealing the rather broad q_{AFM} spot (see red dashed circles). The nanoscale spatial structure of the underlying spin order is more clearly disclosed by

using gaussian pass filters to remove all signal but that around q_{AFM} from the FFT and looking at the inverse FFT of this image (Fig. 6b). It unveils worm-shaped domains of commensurate DDS spin order with a width of ~4 nm. Across the domain walls between neighboring domains (black lines), the spin contrast changes from blue to red or vice versa along the *b*-direction, indicating π-phase slips in the spin order between neighboring domains. Note that the spin order seems to leak across the structural B-type domain boundary as the transition between the two orientations of the DDS spin order is not as abrupt as indicated by the vertical dashed line in Fig. 6b. Figure 6e, f show the same procedures applied to the SP-STM image of the sample with the critical excess Fe content. Most striking, the FFTs, both to the left and to the right of the B-type domain boundary, now reveal an additional q vector which has the same length as q_{AFM} but is rotated by 90°. The inverse FFT in Fig. 6e shows that it originates from three types of irregular nanoscale domains: in the first type the DDS spin order is along the usual *b*-direction; in the second type it is rotated by 90°; finally, in a third type, both orientations overlap such that effectively a plaquette spin order[12,15,26] dominates. Between neighboring domains, i.e., across the black lines, we can still observe the π-phase slips.

DISCUSSION

Finally, we discuss the interpretation of these experimental findings with regard to the existing literature.[8,10–16,21,23] For the $Fe_{1.08}Te$ sample, there are probably two competing processes; one tries to keep the commensurate DDS spin order present inside the domains, while the other tries to make the order incommensurate by the formation of π-phase shifts. This behavior is consistent with the proposed so called lock-in transition between commensurate and incommensurate order driven by the competition of single-ion magnetic anisotropy favoring commensurate DDS order and exchange interaction favoring incommensurate DDS order.[27] For $Fe_{1.12}Te$, the spin order is obviously instable against plaquette order and spatially very inhomogeneous. This finding is consistent with recent theories suggesting that plaquette order is favored by a larger amount of interstitial Fe atoms and that the spin order additionally depends on the distance of the interstitial Fe atoms to the Fe plane.[15] The latter entity might be locally varied in our sample as provoked by the plaquette order domains (Fig. 6e) and the structural chevron pattern (dashed lines in Fig. 6d). Note, however, that there is no obvious correlation between the chevron pattern and the spin order (dashed lines in Fig. 6e). It is, therefore, most likely that the irregular narrow chevron pattern observed in the $Fe_{1.12}Te$ samples still originates from neighbouring $\mathcal{M}$ stripes rotated by 180°, and that the spin order changes between DDS and plaquette due to an inhomogeneous distribution of interstitial Fe. On the other hand, the narrow width of the $\mathcal{M}$ stripes along the *a*-direction (~4 nm) might induce additional strain resulting in a crystal structure that changes between almost $\mathcal{M}$ toward $\mathcal{O}$ accross the stripes which would resolve the apparent mixed phase suggested by spatially averaging techniques.[8,21]

To summarize, we have presented the simultaneous experimental investigation of the spatially resolved structure and magnetism in $Fe_{1+y}Te$ which is continuously driven through the magnetic phase transition. For low excess iron content, a chevron pattern appears due to the four rotational $\mathcal{M}$ domains each containing an irregular pattern of locally commensurate DDS spin order domains with π-phase slips between neighboring domains. For an excess iron content in the critical regime ($y = 0.12$), we found evidence for a mixing between DDS spin order in the two possible orientations and plaquette order in a very narrow, possibly strained, $\mathcal{M}$ chevron phase. Our results show how the structural and spin orders in the parent compound of a prototypical Fe-based superconductor are intertwined on the atomic scale. Moreover, they reveal a drastic shrinking of the structural domain size by slow phase transitions (Fig. 4e). While the used technique is surface sensitive, the observed domain structure is most likely reflecting the structure in the bulk of the material, as we have seen that surface defects do not show any influence on the structural domains (Fig. 4e, f). Our methodology therefore represents a pathway to investigate how spin and structural order can be established or suppressed by an appropriate treatment of the sample. As suppression of the DDS spin order in Fe-based materials toward collinear antiferromagnetic spin order usually leads to the promotion of superconductivity,[15] a similar study for the related superconducting compound $Fe_{1+y}Se_xTe_{1-x}$ will give profound insights into the question how superconductivity emerges from the spin ordered phase.

METHODS

SP-STM

Temperature-dependent SP-STM measurements were performed using a home-built variable temperature STM[28,29] located in a commercially available ultra-high vacuum (UHV) system, in which the samples have been treated prior to the presented measurements. The base pressure of the STM chamber was kept below 1×10^{-10} mbar at all times. The tip and sample temperatures were controlled by a liquid Helium (He) flow cryostat covering temperatures from room temperature down to 30 K. The used chromium (Cr) bulk tip was electrochemically etched ex situ and treated in situ via field emission against a W(110) substrate before measuring.[30] In order to finally achieve a stable spin contrast, the tip "apex" was repeatedly changed by applying rather high voltages of 1–2 V and high currents of 1–2 nA, while scanning the $Fe_{1+y}Te$ surface, preferably when crossing a step edge. Due to the lack of magnetic field dependent data for the measurements shown here, the absolute orientation of the spin sensitivity of the used tip is unknown. However, the fact that we observe a strong DDS spin contrast for the low doped samples proves that the tip is sensitive to the sample magnetization component in the direction of the orientation of the spins in the DDS spin structure.[17] SP-STM images were recorded in constant-current mode at a temperature T, using a tunneling current (I_t) and sample bias (V_s), as stated individually for each image. The crystallographic orientation of the surface, known from atomically resolved STM images, is indicated by arrows in the constant-current STM images. Note that due to temperature drift and scanner creep effects, there is a distortion of the STM images along the slow scanning direction (vertical) resulting in a deviation of the angle between q_a and q_b from 90°. These effects also lead to a larger systematic error in the determination of the angle θ_{STM} that has been estimated to 10% by graphic rectification of images using the atomic resolution of the almost square surface Te lattice. The systematic errors in δ_{STM} and β_{STM} are dominated by the uncertainty in the z calibration of the scanner piezo.

Magnetic susceptibility and X-ray diffraction measurements

Magnetic susceptibility and SC-XRD measurements were performed on $Fe_{1.08}Te$ and $Fe_{1.12}Te$ crystal pieces originating from the same region of the $Fe_{1+y}Te$ boule as the crystals investigated by STM. Thereby, we took special care to ensure the same composition, i.e., an identical excess Fe content y, of the samples investigated by all used methods. The magnetic susceptibility was measured on a quantum design physical property measurement system equipped with a vibrating sample magnetometer as field cooling and heating cycles in a magnetic field of 0.1 T.

Sample preparation

$Fe_{1+y}Te$ single crystal boules were grown by the Stockbarger–Bridgman method using iron pieces (99.99%) and pieces of tellurium ingot (99.999%). The starting materials with nominal compositions $y = 0$ and $y = 0.03$ each had a total mass of 12 g and were loaded in quartz tubes (ID 8 mm) with a conical tip and evacuated to a pressure of less than 4×10^{-4} mbar and then sealed. The tube was then sealed in a larger quartz tube (ID 12 mm). A prereaction was performed at 1000 °C for 24 h to ensure homogeneity of the starting material. The tube was then inserted in a vertical tube furnace maintained at a fixed temperature of 965 °C and translated out of the hot zone at a rate of 2 mm h^{-1}. At the melting point of 914 °C the thermal gradient was measured to be 25 °C cm^{-1}. The obtained crystal boule could

be cleaved across the entire diameter using a razor blade. Single crystal slabs with composition $Fe_{1.08}Te$ and $Fe_{1.12}Te$ as determined by inductively coupled plasma optical emission spectrometry were selected for further characterization by STM.

Two $Fe_{1+y}Te$ crystals were cleaved several times at ambient conditions by the scotch tape method before introducing them into the UHV chamber. Subsequently, the $Fe_{1+y}Te$ crystals were cleaved with the same method under UHV conditions ($p < 10^{-10}$ mbar). This results in a clean, uncontaminated, and atomically flat surface.[31] The cleaving procedure splits the sample along the weakly bound van der Waals gaps between the FeTe layers. This way, STM measurements were always performed on the topmost Te layer. After cleaving under UHV conditions, the $Fe_{1+y}Te$ samples exhibit single Fe atoms at the surface. These are observed as small circular protrusions in the STM images[32] and stem from the excess Fe located within the van der Waals gaps of bulk $Fe_{1+y}Te$ crystals. The Fe atoms can be removed by a mild annealing process. Annealing the cleaved $Fe_{1+y}Te$ crystal at 430 K for 30 min results in a clean $Fe_{1+y}Te$ surface.[31] The surface corrugation and transition temperature T_N of $Fe_{1+y}Te$ are not affected by this mild annealing procedure as verified by the comparison of $Fe_{1.08}Te$ crystals before and after the process. This indicates that the intrinsic excess Fe amount y is not affected by the annealing procedure as well. Merely the topmost excess Fe atoms are removed, thereby improving the quality of the atomically resolved SP-STM images. All presented STM measurements on $Fe_{1.08}Te$ were done on annealed samples except for the data shown in Fig. 4a, b. The investigation of the $Fe_{1.12}Te$ single crystal was carried out on non-annealed samples.

Data availability

The susceptibility and STM data presented in this study are available from the corresponding author upon reasonable request.

ACKNOWLEDGEMENTS

J.Wi. and P.H. acknowledge funding from the German Research Foundation via the DFG priority programme SPP1666 (grant nos. HO 5150/1-2 and WI 3097/2-2). R.W. acknowledges funding via the ERC Advanced Grand ASTONISH (number 338802). J.Wa. and R.W. acknowledge funding from the German Research Foundation via the SFB668. This work was supported by VILLUM FONDEN via the Centre of Excellence for Dirac Materials (grant no. 11744). M.B. acknowledges funding from the Danish National Research Foundation under the grant DNRF93, Center for Materials Crystallography (CMC).

AUTHOR CONTRIBUTIONS

J.Wa., J. Wi., and M.B. designed the experiment. J.Wa. carried out and did the analysis of the SP-STM measurements. M.B. grew the samples, carried out and did the analysis of the magnetic susceptibility, SC-XRD, and ICP-OES measurements. J.Wa. prepared the figures. J.Wa. and J.Wi. wrote the manuscript with contributions from M.B. All authors contributed to the discussion and interpretation of the results, as well as to the discussion of the manuscript.

ADDITIONAL INFORMATION

Competing interests: The authors declare no competing interests.

Publisher's note: Springer Nature remains neutral with regard to jurisdictional claims in published maps and institutional affiliations.

REFERENCES

1. Mizuguchi, Y. & Takano, Y. Review of Fe chalcogenides as the simplest Fe-based superconductor. *J. Phys. Soc. Jpn.* **79**, 10–13 (2010).
2. Hoffman, J. E. Spectroscopic scanning tunneling microscopy insights into Fe-based superconductors. *Rep. Progress. Phys.* **74**, 124513 (2011).
3. Singh, U. R. et al. Spatial inhomogeneity of the superconducting gap and order parameter in $FeSe_{0.4}Te_{0.6}$. *Phys. Rev. B* **88**, 155124 (2013).
4. Kamlapure, A. et al. Spatial variation of the two-fold anisotropic superconducting gap in a monolayer of $FeSe_{0.5}Te_{0.5}$ on a topological insulator. *Phys. Rev. B* **95**, 104509 (2017).
5. Paglione, J. & Greene, R. L. High-temperature superconductivity in iron-based materials. *Nat. Phys.* **6**, 645–658 (2010).
6. Stewart, G. R. Superconductivity in iron compounds. *Rev. Mod. Phys.* **83**, 1589–1652 (2011).
7. Dai, P. Antiferromagnetic order and spin dynamics in iron-based superconductors. *Rev. Mod. Phys.* **87**, 855–896 (2015).
8. Koz, C., Rößler, S., Tsirlin, A. A., Wirth, S. & Schwarz, U. Low-temperature phase diagram of $Fe_{1+y}Te$ studied using x-ray diffraction. *Phys. Rev. B* **88**, 094509 (2013).
9. Subedi, A., Zhang, L., Singh, D. J. & Du, M. H. Density functional study of FeS, FeSe, and FeTe: electronic structure, magnetism, phonons, and superconductivity. *Phys. Rev. B* **78**, 134514 (2008).
10. Ma, F., Ji, W., Hu, J., Lu, Z.-Y. & Xiang, T. First-principles calculations of the electronic structure of tetragonal α-FeTe and α-FeSe crystals: Evidence for a bicollinear antiferromagnetic order. *Phys. Rev. Lett.* **102**, 177003 (2009).
11. Johannes, M. D. & Mazin, I. I. Microscopic origin of magnetism and magnetic interactions in ferropnictides. *Phys. Rev. B* **79**, 220510 (2009).
12. Ducatman, S., Perkins, N. B. & Chubukov, A. Magnetism in parent iron chalcogenides: quantum fluctuations select plaquette order. *Phys. Rev. Lett.* **109**, 157206 (2012).
13. Fang, C., Bernevig, B. A. & Hu, J. Theory of magnetic order in $Fe_{1+y}Te_{1-x}Se_x$. *Europhys. Lett.* **86**, 67005 (2009).
14. Glasbrenner, J. K. et al. Effect of magnetic frustration on nematicity and superconductivity in iron chalcogenides. *Nat. Phys.* **11**, 953– (2015).
15. Tang, S.-C., Ding, M.-C. & Zhang, Y.-Z. Magnetic properties controlled by interstitial or interlayer cations in iron chalcogenides. *Sci. Rep.* **6**, 19031 (2016).
16. Zaliznyak, I. A. et al. Continuous magnetic and structural phase transitions in $Fe_{1+y}Te$. *Phys. Rev. B* **85**, 085105 (2012).
17. Hänke, T. et al. Reorientation of the diagonal double-stripe spin structure at $Fe_{1+y}Te$ bulk and thin-film surfaces. *Nat. Commun.* **8**, 13939 (2017).
18. Bao, W. et al. Tunable ($\delta\pi$, $\delta\pi$)-type antiferromagnetic order in α-Fe(Te,Se) superconductors. *Phys. Rev. Lett.* **102**, 247001 (2009).
19. Rodriguez, E. E. et al. Magnetic-crystallographic phase diagram of the superconducting parent compound $Fe_{1+x}Te$. *Phys. Rev. B* **84**, 064403 (2011).
20. Enayat, M. et al. Real-space imaging of the atomic-scale magnetic structure of $Fe_{1+y}Te$. *Science* **345**, 653–656 (2014).
21. Rodriguez, E. E. et al. Magnetic and structural properties near the Lifshitz point in $Fe_{1+x}Te$. *Phys. Rev. B* **88**, 165110 (2013).
22. Turner, A. M., Wang, F. & Vishwanath, A. Kinetic magnetism and orbital order in iron telluride. *Phys. Rev. B* **80**, 224504 (2009).
23. Fobes, D. et al. Ferro-orbital ordering transition in Iron telluride $Fe_{1+y}Te$. *Phys. Rev. Lett.* **112**, 187202 (2014).
24. Li, S. et al. First-order magnetic and structural phase transitions in $Fe_{1+y}Se_xTe_{1-x}$. *Phys. Rev. B* **79**, 054503 (2009).
25. Koz, C. et al. Pressure-induced successive structural transitions and high-pressure tetragonal phase of $Fe_{1.08}Te$. *Phys. Rev. B* **86**, 094505 (2012).
26. Zaliznyak, I. A. et al. Unconventional temperature enhanced magnetism in $Fe_{1.1}Te$. *Phys. Rev. Lett.* **107**, 216403 (2011).
27. Parshall, D. et al. Competition between commensurate and incommensurate magnetic ordering in $Fe_{1+y}Te$. *Phys. Rev. B* **85**, 140515 (2012).
28. Eich, A. et al. Intra- and interband electron scattering in a hybrid topological insulator: Bismuth bilayer on Bi_2Se_3. *Phys. Rev. B* **90**, 155414 (2014).
29. Warmuth, J. et al. Band-gap engineering by Bi intercalation of graphene on Ir (111). *Phys. Rev. B* **93**, 165437 (2016).
30. Manna, S. et al. Interfacial superconductivity in a bi-collinear antiferromagnetically ordered FeTe monolayer on a topological insulator. *Nat. Commun.* **8**, 14074 (2017).
31. Arnold, F. et al. Electronic structure of $Fe_{1.08}Te$ bulk crystals and epitaxial FeTe thin films on Bi_2Te_3. *J. Phys. Condens. Matter* **30**, 065502 (2018).
32. He, X. et al. Nanoscale chemical phase separation in $FeTe_{0.55}Se_{0.45}$ as seen via scanning tunneling spectroscopy. *Phys. Rev. B* **83**, 220502 (2011).